scientific reports

Check for updates

OPEN

Comparison of multi echo T_2 relaxation and steady state approaches for myelin imaging in the central nervous system

Adam V. Dvorak[1,2]✉, Emil Ljungberg[3], Irene M. Vavasour[1,4], Lisa Eunyoung Lee[5], Shawna Abel[5], David K. B. Li[4,5], Anthony Traboulsee[5], Alex L. MacKay[1,4] & Shannon H. Kolind[1,2,4,5]

The traditional approach for measuring myelin-associated water with quantitative magnetic resonance imaging (MRI) uses multi-echo T_2 relaxation data to calculate the myelin water fraction (MWF). A fundamentally different approach, abbreviated "mcDESPOT", uses a more efficient steady-state acquisition to generate an equivalent metric (f_M). Although previous studies have demonstrated inherent instability and bias in the complex mcDESPOT analysis procedure, f_M has often been used as a surrogate for MWF. We produced and compared multivariate atlases of MWF and f_M in healthy human brain and cervical spinal cord (available online) and compared their ability to detect multiple sclerosis pathology. A significant bias was found in all regions ($p < 10^{-5}$), albeit reversed for spinal cord (f_M-MWF = −3.4%) compared to brain (+6.2%). MWF and f_M followed an approximately linear relationship for regions with MWF < ~10%. For MWF > ~10%, the relationship broke down and f_M no longer increased in tandem with MWF. For multiple sclerosis patients, MWF and f_M Z score maps showed overlapping areas of low Z score and similar trends between patients and brain regions, although those of f_M generally had greater spatial extent and magnitude of severity. These results will guide future choice of myelin-sensitive quantitative MRI and improve interpretation of studies using either myelin imaging approach.

Quantitative magnetic resonance imaging (MRI) techniques are developed with the aim of being specific to certain features of tissue microstructure. In the case of myelin water imaging, the water trapped between myelin bilayers can be used as a biomarker for myelin content.

The original method for myelin water imaging was a multi-echo spin-echo T_2 relaxation acquisition, which can quantify signal contributions from different characteristic T_2 relaxation times, such as those associated with water trapped between myelin lipid bilayers ($T_2 < 40$ ms at 3 T) or water within intra- and extra-cellular spaces (40 ms < T_2 < 200 ms)[1]. The myelin water fraction (MWF) metric can then be calculated as the signal contribution from T_2 relaxation times associated with myelin water divided by the total signal. Although this model neglects the presence of non-aqueous protons and the effects of magnetization exchange between water pools[2,3], the MWF has been shown to correlate well with quantitative histopathologic measures of myelin density[4–6]. A multi-echo 3D GRAdient-echo and Spin-Echo (GRASE) sequence can be used to reduce acquisition time by a factor of 3 with a negligible reduction in the resulting MWF map quality compared to a multi-echo spin-echo sequence[7,8].

The value of an in-vivo myelin biomarker has motivated the development of alternative approaches to myelin imaging. One commonly used alternative is the multi-component Driven-Equilibrium Single-Pulse Observation of T_1 and T_2 (mcDESPOT) technique, which is based on a series of steady-state acquisitions[9]. Spoiled gradient recalled echo (SPGR), inversion-recovery-prepared SPGR (IRSPGR) and balanced steady-state free precession (bSSFP) images are acquired with a range of flip angles (FA), from which T_1 and T_2 can be estimated. The mcDESPOT analysis framework requires fitting the data to a large number of parameters simultaneously,

[1]Physics and Astronomy, University of British Columbia, Vancouver, BC, Canada. [2]International Collaboration on Repair Discoveries (ICORD), University of British Columbia, Vancouver, BC, Canada. [3]Department of Neuroimaging, Institute of Psychiatry, Psychology & Neuroscience, King's College London, London, UK. [4]Radiology, University of British Columbia, Vancouver, BC, Canada. [5]Medicine (Neurology), University of British Columbia, Vancouver, BC, Canada. ✉email: adam.dvorak@ubc.ca

including separate, exchanging T_1 and T_2 components for myelin-associated and intra-/extra-cellular water, which facilitates calculation of the mcDESPOT myelin water fraction (f_M). Compared to myelin imaging with multi-echo T_2 relaxation, mcDESPOT is appealing for its intrinsic acquisition efficiency[10], which can be leveraged to improve coverage, resolution, or acquisition time, and for its additional quantitative metrics, such as T_1 and exchange rate constants, which can provide supplemental information.

Potential inaccuracies or biases of the GRASE and mcDESPOT analysis procedures have previously been explored. Multi-component T_2 analysis of GRASE, or any multi-echo T_2 relaxation data, relies on suitable analysis parameters and sufficient data signal-to-noise ratio for MWF values to stabilize[11]. mcDESPOT analysis requires accurate parameter fitting boundaries to be defined, but even then has been criticized for non-unique solutions and inherent, unpredictable bias in the fitting procedure[12–15].

Similarly, both acquisitions have a set of MR-signal related potential confounds for myelin imaging, which have been reasonably well studied[16–24]. Previous studies have found differences between MWF and f_M in brain tissue, with mcDESPOT providing consistently higher myelin estimates, especially in gray matter (GM), and a much more uniform distribution of values, especially in white matter (WM)[24–26]. However, MWF and f_M values reported in cervical spinal cord are relatively similar[27,28], which is surprising given their disparity in the brain. This difference between brain and spinal cord could be related to the influence of MR physics related confounding factors, bias in analysis procedures, differences in cyto-architecture between brain and spinal cord, or likely a combination of the above.

Despite these differences, both GRASE and mcDESPOT have individually demonstrated sensitivity to pathology and developmental changes in the central nervous system, often with conclusions that corroborate one another[26,29–32]. Previous work has reported a significant, moderately strong correlation between MWF and f_M in brain tissue[26], further suggesting that steady-state approaches can serve as effective alternatives to multi-echo T_2 relaxation myelin imaging.

However, as previously reported values suggest that this relationship might not hold in the spinal cord, a direct comparison with spinal cord data would be of great value as it could strengthen or contradict the purported correspondence between MWF and f_M.

In this study, we perform the first direct comparison of multi-echo T_2 relaxation (GRASE) and steady-state (mcDESPOT) myelin imaging in both the brain and cervical spinal cord in a cohort of healthy participants. Our comparison is supplemented with data in the context of demyelinating disease pathology, analyzed on an individual basis for people with multiple sclerosis. The goals of this study are to:

- create atlases of normative reference MWF and f_M values for both brain and cervical spinal cord;
- use atlas-based methods to compare myelin imaging approaches with minimal influence from biological variation and measurement noise;
- improve characterisation of the relationship between MWF and f_M, by comparing values across a diverse range of tissue, including healthy and diseased brain and spinal cord.

Results

Five of the 28 participants had to be excluded from the MWF and f_M spinal cord atlases, due to imaging artefacts that rendered their GRASE or mcDESPOT data unusable.

Mean atlas ROI values. Table 1 provides the mean and standard deviation (SD) of voxel values within each brain and spinal cord region of interest (ROI), calculated for the mean MWF and f_M atlases. Mean MWF and f_M ROI values across all healthy control participants differed significantly ($p < 10^{-5}$) for all ROIs. f_M values were higher than MWF in all brain ROIs by a factor of ~ 2, except for the posterior internal capsule where values were more similar ($f_M = 19.5 \pm 1.2\%$, $MWF = 17.6 \pm 4.0\%$) and the caudate where f_M was larger by a factor of ~ 3 ($f_M = 10.0 \pm 3.3\%$, $MWF = 3.0 \pm 1.8\%$). In spinal cord, f_M was lower than MWF in all ROIs except GM and the absolute difference between f_M and MWF values was smaller than in brain.

Healthy participant ROI values. In Fig. 1 mean MWF and f_M values within each ROI, for each healthy participant, are displayed. Figure 1A shows f_M plotted against MWF, for each ROI value. The Bland–Altman plot in Fig. 1B shows the difference between each MWF and f_M ROI value plotted against their mean.

There was an approximately linear relationship between MWF and f_M for brain regions (circle data points in Fig. 1A) with MWF < ~ 10%. The linear MWF-f_M relationship did not hold in the spinal cord, or in brain regions with MWF > ~ 10%. The non-linearity between f_M and MWF appears qualitatively consistent across participants, with a tight spread of data points following the same distinct pattern. The intra-subject, intra-ROI variability of each metric, indicated by standard deviation uncertainty bars in Fig. 1A, is small compared to the range of f_M and MWF values and could not account for the non-linear relationship.

In the spinal cord, MWF spanned a large range of values (12–30%) whereas f_M had little variation (16–23%). A systematic bias exists between MWF and f_M values, but with opposite sign for brain (mean WM&GM f_M-MWF = 6.2%) compared to spinal cord (mean whole cord f_M-MWF = − 3.4%).

Templates and atlases. Representative slices of the anatomical templates, T_1-weighted (T_1w) for brain and T_2*-weighted (T_2*w) for spinal cord, voxel-wise mean MWF and f_M atlases, and voxel-wise SD MWF and f_M atlases are displayed in Fig. 2A for brain and Fig. 2B for spinal cord. As observed in Fig. 1A, there is a larger dynamic range in the myelin estimates with MWF compared to f_M. In the mean MWF atlas of the spinal cord,

ROI	MWF (%)	f_M (%)	ROI volume
	Mean ± SD	Mean ± SD	Number of voxels
All WM&GM	5.7 ± 5.4	11.9 ± 5.5	1,239,957
Brain white matter			
All WM	8.0 ± 4.9	16.8 ± 4.1	538,746
All JHU	11.5 ± 4.5	19.9 ± 2.7	78,903
Genu	9.1 ± 2.3	20.0 ± 3.0	5260
Splenium	13.4 ± 2.8	20.4 ± 3.1	7527
CC	11.1 ± 3.0	19.6 ± 3.0	21,435
Posterior internal capsule	17.6 ± 4.0	19.5 ± 1.2	5437
Brain lobe white matter			
Frontal	7.1 ± 3.5	17.6 ± 3.4	115,698
Occipital	7.3 ± 3.2	16.0 ± 3.9	72,205
Parietal	8.3 ± 3.7	17.8 ± 3.6	100,925
Temporal	6.8 ± 2.9	16.4 ± 3.7	45,173
Brain gray matter			
All GM	4.1 ± 5.2	8.1 ± 2.7	701,211
Cortical	3.7 ± 4.1	8.7 ± 2.8	445,356
Caudate	3.0 ± 1.8	10.0 ± 3.3	8130
Thalamus	7.4 ± 5.2	13.2 ± 3.7	14,105
Putamen	5.0 ± 3.8	12.0 ± 2.6	13,748
Spinal cord			
Whole	22.1 ± 5.7	18.7 ± 2.9	18,673
All WM	23.8 ± 4.4	18.6 ± 3.2	14,614
All GM	15.7 ± 5.1	19.0 ± 1.0	4059
Dorsal column	25.6 ± 4.6	19.2 ± 2.5	5541
Lateral funiculi	22.8 ± 3.9	18.3 ± 3.3	7235

Table 1. Mean and standard deviation (SD) of voxels within each region of interest (ROI) for the mean myelin water fraction atlases from multi-echo T_2 relaxation (MWF) and steady-state (f_M) approaches. ROI volumes are also provided. A paired, two-tailed t test found significantly different MWF and f_M ROI values ($p < 10^{-5}$) across healthy control participants, for all ROIs. Brain ROIs include all white matter (WM), all gray matter (GM) and combined WM&GM from T_1w image segmentations, along with 9 additional WM ROIs (all JHU white matter labels combined, genu of corpus callosum, splenium of corpus callosum, whole corpus callosum (CC), posterior internal capsule, and frontal, occipital, parietal, and temporal lobes masked to WM), and 4 additional GM ROIs (cortical GM, caudate, thalamus, and putamen). Spinal cord ROIs include the whole cord, WM, GM, dorsal column, and lateral funiculi.

structures such as gray matter and dorsal column can be identified clearly. The templates, mean and SD atlases, and ROIs analyzed for MWF and f_M in brain and spinal cord are openly available online[33].

Z scores. Representative slices of Z score maps comparing relapsing–remitting multiple sclerosis (RRMS) and primary progressive multiple sclerosis (PPMS) MWF and f_M to the healthy participant atlases are shown in Fig. 3 for brain and for spinal cord. The RRMS Z score maps, Fig. 3A, show evidence of some small, focal areas of deficient MWF and f_M compared to controls, likely corresponding to the location of lesions. The PPMS Z score maps, Fig. 3B, show widespread regions of low Z score for both MWF and f_M in both brain and spinal cord.

In Fig. 3, histograms for brain and cord of each patient show similar distributions of Z score values for MWF and f_M, with the largest differences visible in the extremes of the Z score range for PPMS. For RRMS, a slight shift towards lower values is apparent for the MWF Z score histogram, compared to f_M. For PPMS, the MWF Z score maps are generally less extreme in terms of both spatial extent and statistical magnitude compared to those of f_M. While PPMS Z score maps suggest that f_M has greater sensitivity to the presence of pathological tissue changes, RRMS Z score histograms suggest that MWF may better identify subtle changes outside regions of more-extreme pathology. Regions of deficient MWF Z score are generally highlighted on the corresponding f_M Z score map, although this congruity appears to be more consistent in brain.

Discussion

The atlas-based methods employed here provided an effective means of reducing biological variations and measurement noise present within and between individual participant quantitative metric maps. In addition to facilitating the creation of Z score maps, atlas-based methods provide increased statistical power for characterizing discrepancies between the quantitative myelin fraction metrics obtained with GRASE and mcDESPOT. The smooth, "high SNR" appearance of the atlases in Fig. 2 provide clear depictions of representative values expected

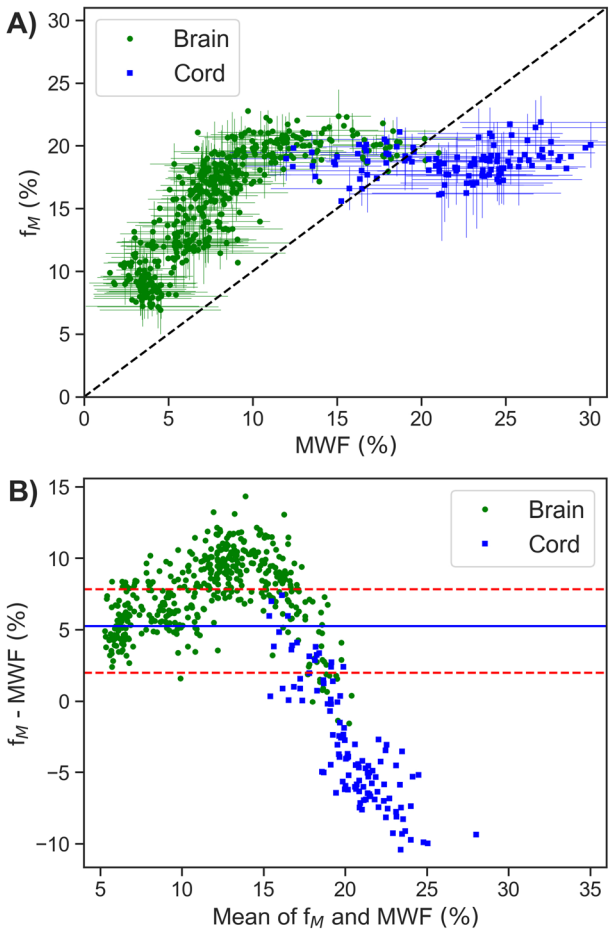

Figure 1. Mean myelin water fraction values for each region of interest (ROI), for each healthy control, from multi-echo T_2 relaxation (MWF) and steady-state (f_M) approaches. (**A**) A correlation plot between MWF and f_M, where the dotted line indicates the line of unity. Linear regression was omitted, due to the clearly non-linear relationship between MWF and f_M. Uncertainty bars indicate the standard deviation of voxel values for that subject and ROI, only plotted for every third data point to improve visibility. (**B**) Bland Altman plot displaying the mean of MWF and f_M values on the x axis and the difference on the y axis. The solid line indicates the mean bias (difference) of all data points (+5.3%). Dotted lines indicate positive and negative 95% limits of agreement; +7.8% and +2.0%, respectively. ROIs include all white matter (WM), all gray matter (GM) and combined WM&GM from T_1w image segmentations, along with 9 additional WM ROIs (all JHU white matter labels combined, genu of corpus callosum, splenium of corpus callosum, whole corpus callosum, posterior internal capsule, and frontal, occipital, parietal, and temporal lobes masked to WM), and 4 additional GM ROIs (cortical GM, caudate, thalamus, and putamen). Spinal cord ROIs include the whole cord, WM, GM, dorsal column, and lateral funiculi.

from each imaging modality. They can also serve as a reference for how MWF and f_M values are expected to differ throughout commonly investigated regions in the central nervous system. The MWF and f_M atlases are openly available and provide normative reference data to increase statistical power for future studies with limited ability to recruit and collect data from healthy controls.

Although previous studies have compared MWF and f_M in the brain, this is the first comparison of MWF and f_M values in both the brain and spinal cord. Our combined analysis yielded some consequential results, especially when interpreting spinal cord results in concert with those from brain. First, the absolute difference in magnitude between myelin-related metric values produced by multi-echo T_2 relaxation and steady-state approaches is much smaller in spinal cord than in brain. Despite having more-similar magnitudes than in brain, MWF and f_M in the spinal cord bear almost no correspondence. Secondly, the average bias between GRASE and mcDESPOT is reversed in spinal cord (mean whole cord f_M-MWF = − 3.4%) compared to brain (mean WM&GM f_M-MWF = 6.2%). The inversion of the MWF versus f_M bias between brain and spinal cord is clearly depicted by the individual participant mean ROI values plotted in Fig. 1A, where most brain and spinal cord data points lie on opposite sides of the line of unity.

Although comparisons in human brain have shown significant, moderately strong correlations between MWF and f_M[26], the same linear relationship does not hold in the spinal cord. Figure 1A suggests that this relationship

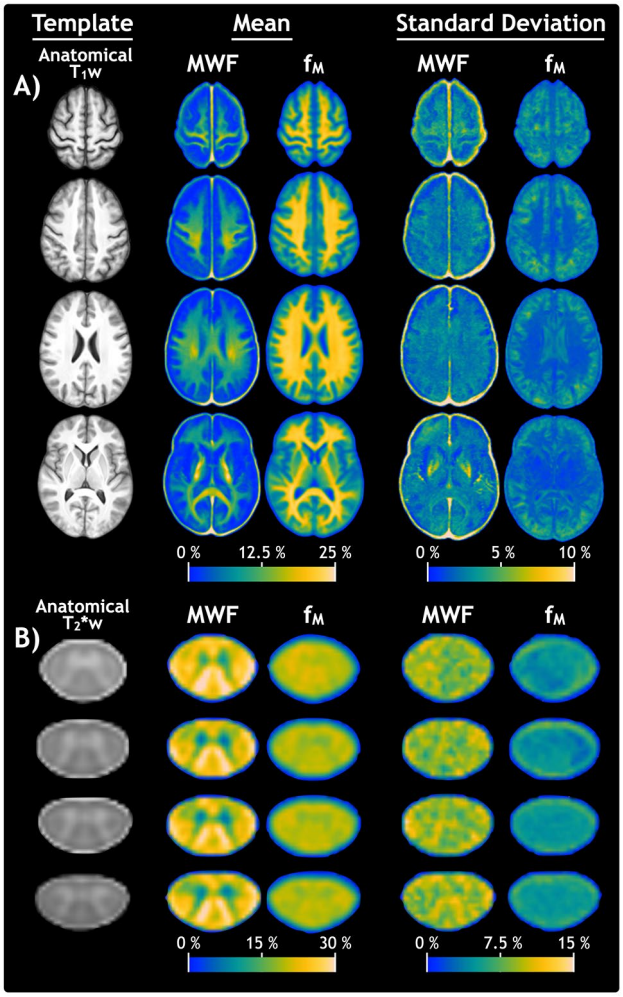

Figure 2. Representative slices of the anatomical templates as well as quantitative atlases for the myelin water fraction from multi-echo T_2 relaxation (MWF) and steady-state (f_M) approaches, for the (**A**) brain and (**B**) C2 and C3 level of the cervical spinal cord. From left to right, columns display the: anatomical template, mean atlases, and the standard deviation atlases. Mean and standard deviation atlases are calculated voxel-wise across 28 participants for brain and 23 participants for spinal cord.

actually begins to break down in brain regions as well. Specifically, MWF and f_M do not appear to be correlated in regions with MWF > ~ 10%, where f_M no longer increases in tandem with MWF. In hindsight, this is visible in some brain regions examined by previous studies[26,34], but the magnitude and extent of the incongruity between the two methods is made clear by our unified, direct comparison with both brain and spinal cord data.

Our atlas ROI results (Table 1) show that MWF is lower than f_M throughout all investigated brain ROIs, in agreement with previous studies that compared values in the brain[24–26]. Lack of contrast in f_M between WM ROIs, as demonstrated by Table 1 values and qualitatively by mean f_M atlases in Fig. 2, also matches expectations based on previous brain studies with mcDESPOT[24–26].

Previous work has provided evidence that myelin content within human brain WM is heterogeneous. Aboitiz et al. studied the corpus callosum in post-mortem human brain using the Loyez histological stain for myelin and electron microscopy[35]. They found that the genu had a smaller median axon diameter (0.6 µm) compared to the splenium (1.0 µm), which is expected to correspond with lower oligodendrocyte proliferation and myelin content[35]. They also found a high percentage of unmyelinated fibers in the genu (16%) compared to the rest of the corpus callosum (< 5%)[35]. Both of these findings support the expectation of lower myelin content in the genu, compared to the splenium, which we found reflected in our results for MWF but not for f_M. In more recent studies using histological staining markers for myelin, the optical density of Luxol fast blue showed regional variation by factors > 2 within non-lesional WM, albeit in MS brain tissue where pathological changes could increase stain contrast[5,6]. Bürgel et al. demonstrated strong regional contrast in WM myelination when they used a modified Heidenhain–Woelcke stain[36] to distinguish major tracts (including the corticospinal tract, optic and acoustic radiations, fornix, cingulum, corpus callosum, superior longitudinal, superior and inferior occipito-frontal and uncinate fascicles) in 10 post-mortem brains by their relative degrees of myelination[37]. Therefore, the low contrast of f_M within WM is likely not representative of myelin content but rather could relate to a confounding factor for

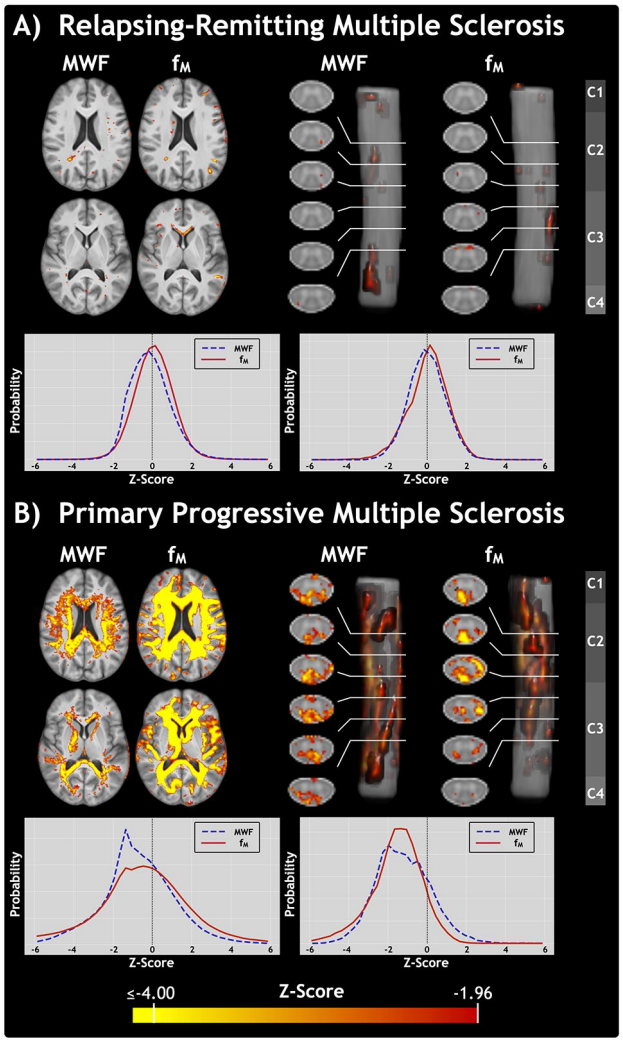

Figure 3. Representative slices of Z score maps for the myelin water fraction from multi-echo T_2 relaxation (MWF) and steady-state (f_M) approaches. Deficient Z scores, with $Z \leq -1.96$, are superimposed on the anatomical templates for (**A**) one participant living with relapsing–remitting multiple sclerosis (female, age 26 years, expanded disability status scale (EDSS) 1.5, disease duration 3 years) and (**B**) one with primary progressive multiple sclerosis (female, age 64 years, EDSS 8.5, disease duration 29 years). From left to right, columns display: axial brain slices, axial cervical spinal cord slices, sagittal cervical cord views, and the corresponding vertebral levels of the cord. For brain and cord of each patient, histograms are plotted to show the distribution of Z score values for MWF (dashed blue line) and f_M (solid red line). Z scores were calculated as the difference between multiple sclerosis metric values and the mean atlas, divided by the standard deviation atlas.

mcDESPOT, such as the increased influence of magnetization transfer. Similarly to f_M, magnetization transfer ratio maps show relatively little contrast between WM regions compared to MWF[38], but studies investigating the relationship between magnetization transfer and mcDESPOT have not been able to confirm that magnetization transfer has a prominent influence on f_M values[24].

Our GRASE and mcDESPOT values agree with mean whole cord MWF and f_M values reported previously by our group in healthy cervical spinal cord: 22.1% versus 22.9% reported by Ljungberg et al.[27] and 18.7% versus 20.5% reported by Kolind et al.[28]. In our study, WM accounted for 78% of the spinal cord volume, compared to 43% of brain tissue volume. As a result, higher mean MWF and f_M can generally be expected across the whole spinal cord. Although this does not explain higher MWF in both WM and GM individually, previous studies have reported approximately 2.5 times higher myelin content in the cord, compared to the cerebrum, of rat nervous system[39], providing a precedent for a similar pattern to exist in human tissue.

There are many possible explanations for the low f_M in the spinal cord, compared to expectations from the brain. Like all quantitative MRI techniques, GRASE and mcDESPOT each have their own set of confounds, which could affect the results more or less in the spinal cord, causing the relationship between MWF and f_M to change.

GRASE is expected to have some magnetization transfer effects due to repeated refocusing pulses throughout the echo train[40]. For mcDESPOT, the short, high-amplitude excitation pulses used to acquire SPGR and bSSFP

data minimize undesirable finite radio-frequency pulse effects but increase the effects of magnetization transfer. By sensitizing the signal to macromolecular protons present in biological tissue, magnetization transfer can have a profound effect on estimates of T_1 and T_2 relaxation values[41–43]. Modified versions of mcDESPOT have been introduced with additional model parameters in an attempt to quantify and correct for magnetization transfer[44]. Upon investigation, Zhang et al. confirmed that removal of magnetization transfer has a strong effect on bSSFP signal curves. However, values for f_M remained much higher than MWF, suggesting that magnetization transfer does not drive the MWF-f_M difference in brain. The fact that signal changes did not propagate into the expected parameter changes helped motivate subsequent investigation into the mcDESPOT analysis procedure.

The GRASE MWF is generally underestimated in regions with very low signal contribution from myelin water, such as cortical GM brain regions, where there is insufficient signal-to-noise for accurate myelin water quantification[45]. The multi-component T_2 analysis used with GRASE ignores the effects of T_1 relaxation. Using a short repetition time (TR) with GRASE could therefore artificially increase MWF values, due to additional T_1 weighting. However, our TR of 1073 ms is not expected to have a large influence on MWF and does not explain the discrepancy with f_M cord values[46]. Recent studies have shown that the MWF will decrease if the inter-compartmental exchange rate between myelin water and intra/extra-cellular water increases[40,47]. Therefore, GRASE MWF values may be underestimated, especially in regions with small axons and thin myelin sheaths, where an increase in inter-compartmental exchange can be expected[48]. In comparison, mcDESPOT should be immune to this effect, assuming the analysis includes and accurately estimates the myelin water residence time parameter that is intended to account for exchange. However, omitting exchange from the mcDESPOT model so it is not accounted for, as with GRASE, does not remove the discrepancy between MWF and f_M values[25].

The caveat that the residence time must be accurately estimated becomes problematic in the context of recent studies evaluating the mcDESPOT analysis. Degeneracy of parameter solutions in mcDESPOT, a fundamental problem afflicting many MRI microstructure mapping techniques[49], was first shown by Lankford and Does studying mcDESPOT precision with Cramér-Rao lower bounds[12]. Imprecision of mcDESPOT solutions has been further demonstrated by Zhang et al. and Bouhrara et al., who both showed flat residual plots of mcDESPOT parameter fits[14,25]. This can result in substantial instability in metric values, especially for moderate or low signal-to-noise data[14]. They also showed that the instability could be reduced by removing fit parameters, specifically by ignoring the effects of exchange[25].

A recent investigation by West et al. further showed that mcDESPOT solutions are inaccurate and imprecise when exchange is included in the model[15]. As in previous work, they found that ignoring exchange improved the stability of the analysis, but at the cost of significantly biased results[15]. West et al. also found that changes in mcDESPOT analysis results were non-linear with respect to changes in their true values, and that changing a single parameter could induce marked changes in other, static parameters[15]. For example, a change in the T_1 or T_2 value of intra-/extra-cellular water can result in a large change in f_M results, even when the true value of f_M has not changed[15]. The notable sensitivity of f_M to pathological tissue differences could be in part explained by certain pathology-related changes to T_1 or T_2 inducing a large, non-linear response in the f_M results[15].

West et al. suggested that unpredictable bias in mcDESPOT results can be at least partially mitigated by the use of consistent acquisition and analysis parameters[15]. However, our results suggest that even with consistent acquisition and analysis conditions, changes in signal characteristics due to the presence of pathology (multiple sclerosis) or unique tissue structures (spinal cord) propagate into f_M values in a way that does not consistently reflect MWF values.

The anatomical structure of the spinal cord likely plays an important role in our observed breakdown of the MWF-f_M relationship as well as the lack of contrast observed in our f_M spinal cord results. The non-linear behaviour of the mcDESPOT analysis procedure could lead to biased results that do not necessarily reflect the true underlying values. Spinal cord WM is similar to that of corpus callosum in the brain, and cord GM is similar to putamen[50]. Therefore, based on contrast between brain values, we can expect that MWF will have more contrast between these regions than f_M. Another consideration is the presence of a low f_M boundary around the cord, larger than that visible for MWF, which is likely related to partial volume effects with cerebrospinal fluid. Partial volume effects could indicate imperfections in the motion correction alignment of each image volume in mcDESPOT data sets. Misalignment from motion relates to the fact that mcDESPOT acquires central k-space data separately for each image volume, spread across the entire acquisition time, whereas GRASE acquires central k-space data only once. Imperfect alignment of mcDESPOT image volumes would lead to blurred metric maps and reduced contrast between ROIs inside the cord.

MWF and f_M can be used to identify pathology on an individual basis in the brain or spinal cord[51–53]. Here, we demonstrated this using Z score maps, shown in Fig. 3, which showed greater spatial extent and magnitude of severity for mcDESPOT f_M Z scores, compared to those of GRASE MWF.

The high sensitivity of mcDESPOT to pathological differences has been previously demonstrated in the brain by O'Muircheartaigh et al.[26]. Although there is no definitive explanation, the high sensitivity of mcDESPOT is likely due to multiple compounding factors. Relatively low inter-participant f_M variability, as evidenced by the low values of f_M standard deviation between participants (Fig. 2), will tend to amplify Z score values. Another influence may be reduced specificity to myelin, which would grant f_M sensitivity to a variety of pathological changes compared to MWF. Strong correlation (median $\rho = 0.8$) between f_M and quantitative T_1 results from mcDESPOT[26] provides evidence suggesting that f_M is closely related to, if not driven by, relaxation values. Considering this, f_M may not provide enough additional independent, myelin-specific information, compared to the quantitative T_1 metric from DESPOT1-HIFI[20], to justify the increased acquisition time to acquire a full mcDESPOT data set.

Despite their different acquisitions, analyses, and confounding factors, MWF and f_M Z score histogram plots in Fig. 3 show similarity between participants and anatomical structures. Similarity between Z scores and the higher sensitivity of f_M to pathological tissue changes support the interpretation that MWF and f_M are both sensitive to myelin content but that f_M has reduced specificity due the unpredictable, non-linear analysis response to signal

changes. For specificity to myelin, recent technical developments allow acquisition of multi-echo T_2 relaxation data with compressed sensing acceleration, which can provide improved spatial and parametric resolution in less acquisition time, compared to the GRASE sequence presented here[54]. When possible within time constraints, studies should ideally include multiple myelin-sensitive metrics. Additional metrics incorporated in a multimodal imaging approach can provide supplemental information as well as increase confidence in the findings.

In conclusion, we have produced and provided normative reference MWF and f_M atlases for both brain and cervical spinal cord. In comparing these atlases, we found that MWF and f_M follow an approximately linear relationship for regions with MWF < ~10%, above which the relationship breaks down and f_M no longer increases in tandem with MWF. In the context of demyelinating disease pathology, Z score maps from f_M showed greater spatial extent and magnitude of severity. The high sensitivity of f_M is a benefit for detecting pathological changes but is likely related to the mcDESPOT analysis procedure propagating MR signal changes into the f_M results non-linearly and greatly limits the ability to attribute those differences solely to changes in myelin. Despite the fundamental differences in these two techniques, MWF and f_M Z score maps showed overlapping areas of low Z score and similar trends between patients and brain and spinal cord regions. Ultimately, these results will guide future choice of myelin-sensitive quantitative MRI and help improve retrospective interpretation of clinical studies using multi-echo T_2 relaxation or steady-state myelin imaging measures in the context of healthy or diseased central nervous system.

Methods

Ethics. The study operated under ethics approval from the University of British Columbia Clinical Research Ethics Board. All participants provided written informed consent. All methods were performed in accordance with the relevant guidelines and regulations.

Participants. Data were collected from 28 healthy participants without a history of brain or spinal cord disease or injury (10 male and 18 female, mean age 46 years, range 22–65 years). To facilitate comparison of MWF and f_M in the context of pathology, data were also collected from two participants with clinically definite multiple sclerosis fulfilling the 2017 revised MacDonald criteria for diagnosis[55]: one participant with RRMS (female, age 26 years, expanded disability status scale (EDSS[56]) 1.5, disease duration 3 years) and one with PPMS (female, age 64 years, EDSS 8.5, disease duration 29 years).

MRI. Imaging was performed at the UBC MRI Research Centre on a 3.0T MRI scanner (Achieva, Philips Medical Systems, Best, The Netherlands).

Brain MRI were acquired using an 8-channel head coil.

A sagittal 3D T_1-weighted magnetization-prepared rapid gradient-echo image (T_1w) was acquired with TR = 8.1 ms, echo time (TE) = 3.5 ms, inversion time (TI) = 1052 ms, shot interval = 3000 ms, FA = 8°, resolution = 1.0 × 1.0 × 1.0 mm^3, field of view (FOV) = 256 × 256 × 165 mm^3, acquisition time = 6 min 26 s.

Multi-echo T_2 relaxation data were acquired using a 3D multi-echo GRASE sequence with TR = 1073 ms, TE = 8 ms, echo spacing (ΔTE) = 8 ms, 48 echoes, acquired resolution = 1.0 × 2.0 × 5.0 mm^3, reconstructed resolution = 1.0 × 1.0x2.5 mm^3, FOV = 230 × 190 × 100 mm^3, slice oversampling factor = 1.3, sensitivity encoding (SENSE[57]) acceleration factor = 2, and acquisition time = 7 min 31 s.

Steady-state mcDESPOT brain acquisitions consisted of multiple SPGR, a single IRSPGR, and multiple bSSFP images, all acquired with a common resolution = 1.7 × 1.7 × 1.7 mm^3 and FOV = 217 × 217 × 156 mm^3. SPGR were acquired with TR = 6.5 ms, TE = 3.6 ms, and FA = 2, 3, 4, 6, 9, 13, and 18°; IRSPGR with TR = 6.5 ms, TE = 3.2 ms, TI = 450 ms, and FA = 5°; and bSSFP with TR = 5.8 ms, TE = 2.9 ms, FA = 7, 11, 15, 19, 24, 30, and 47° and phase cycling patterns of 0° and 180° for each FA. Total mcDESPOT acquisition time, for all FA and phase cycling patterns, was 9 min 26 s.

Cervical spinal cord imaging used a 6-channel spine coil, with all imaging FOV centred at the C2/C3 level of the cervical spinal cord and angulation aligned with the cord.

An axial 2D multi-slice T_2*-weighted multi-echo gradient echo image (T_2*w) was acquired with TR = 815 ms, TE = 6.5 ms, ΔTE = 8.2 ms, 5 echoes (cumulated on the scanner), FA = 28°, acquired resolution = 0.8 × 0.8 × 2.5 mm^3, reconstructed resolution = 0.3 × 0.3 × 2.5 mm^3, number of slices = 16, slice gap = 0.25 mm, FOV = 150 × 150 × 44 mm^3, and acquisition time = 5 min 7 s.

Multi-echo T_2 relaxation MWI data were acquired as adapted by Ljungberg et al.[27] using a 3D multi-echo GRASE sequence with TR = 1501 ms, TE = 10 ms, ΔTE = 10 ms, 32 echoes, acquired resolution = 0.75 × 0.75 × 5.0 mm^3, reconstructed resolution = 0.63 × 0.63 × 2.5 mm^3, FOV = 180 × 150x40 mm^3, slice oversampling factor = 1.2, SENSE acceleration factor = 2, and acquisition time = 8 min 36 s.

Steady-state mcDESPOT cord acquisitions had a common acquired resolution = 0.75 × 0.75 × 4.00 mm^3, reconstructed resolution = 0.70 × 0.70 × 4.00 mm^3, and FOV = 180 × 201 × 56 mm^3. SPGR were acquired with TR = 5.5 ms, TE = 2.7 ms, and FA = 2, 3, 4, 6, 8, 10, 13, and 18°; IRSPGR with TR = 5.5 ms, TE = 2.7 ms, TI = 350 ms, and FA = 5°; and bSSFP with TR = 10.0 ms, TE = 5.0 ms, FA = 7, 14, 21, 28, 35, 42, and 49° and phase cycling patterns of 0° and 90° for each FA. Total mcDESPOT acquisition time, for all FA and phase cycling patterns, was 6 min 7 s.

The T_1w brain and T_2*w cord images were acquired for their strong white/gray matter contrast, to facilitate alignment of anatomical structures between participants. All acquisitions were performed without cardiac or respiratory triggering. Brain and cord acquisitions for GRASE and mcDESPOT differed slightly due to differences in optimisation of parameters for each application[8,27].

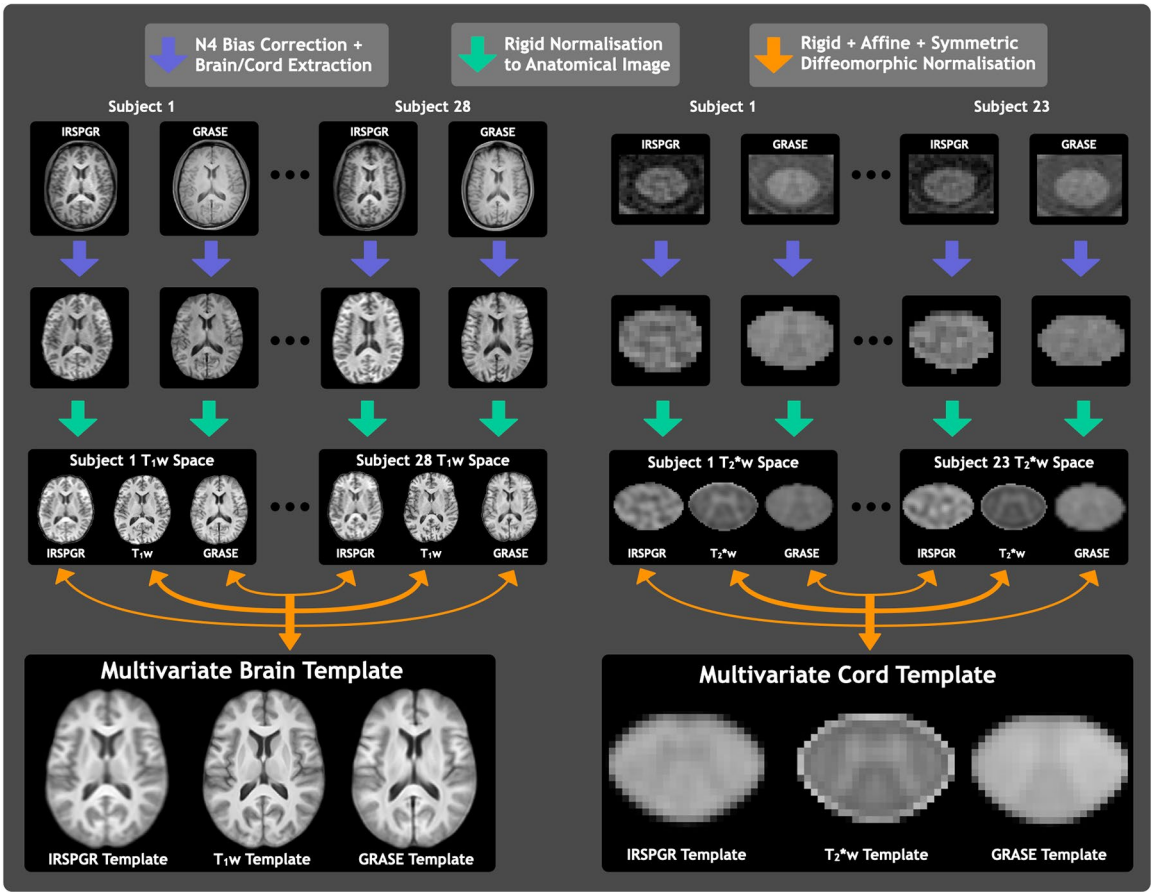

Figure 4. Workflow depicting the multivariate template creation pipeline for brain and cervical spinal cord data. Image registrations used the GRAdient-echo and Spin-Echo (GRASE) echo 1 image from multi-echo T_2 relaxation data, and the inversion-recovery-prepared spoiled gradient recalled echo (IRSPGR) image from the steady-state multi-component Driven-Equilibrium Single-Pulse Observation of T_1 and T_2 (mcDESPOT) data.

Quantitative MRI analysis. GRASE data was analyzed using a temporally-regularized non-negative least squares algorithm with stimulated echo correction (https://mriresearch.med.ubc.ca/news-projects/myelin-water-fraction/), 40 T_2 relaxation delta functions logarithmically spaced from 15 to 2000 ms, 8 refocusing flip angles between 90 and 180°, and a χ^2 regularization factor of 1.02. The MWF was calculated as the fraction of total signal with $15 < T_2 < 40$ ms.

mcDESPOT data underwent motion correction to align the imaging volumes before the DESPOT1-HIFI code was used to obtain an estimated FA correction map from the SPGR and IRSPGR data[20]. Using the FA correction map, mcDESPOT analysis was performed to obtain the f_M. The analysis was matched to that of a previous study on mcDESPOT stability, using a 3-pool model and the same stochastic-region-contraction parameter boundaries: f_M [0.00000001,0.35], myelin water T_1 [300,650] ms, myelin water T_2 [1,30] ms, free water T_1 [700,$T_{1,max}$] ms, free water T_2 [50,165] ms, and myelin water residence time τ [25–600] ms.

Image analysis and template creation. Advanced Normalization Tools software (ANTs), Spinal Cord Toolbox (SCT), and some FMRIB Software Library (FSL) tools were used for image analysis[58–60]. Non-linear registrations used symmetric diffeomorphic normalization (SyN) transformations. To prevent introduction of circularity bias, no quantitative maps were involved in image registrations[61]. Workflow for the multivariate template creation process is outlined in Fig. 4.

All T_1w, GRASE echo 1, and IRSPGR brain images underwent N4 bias field correction for low frequency intensity nonuniformities[62]. Brain segmentations were initialized by registration with the OASIS template and priors[63] then refined using Atropos *n*-tissue segmentation[64]. Each participant's GRASE echo 1 and IRSPGR images were masked to brain tissue before being rigidly aligned with their corresponding T_1w image and masked again using the higher-resolution T_1w brain segmentation.

For spinal cord images, cord segmentations were generated for each image modality using T_2*w, GRASE echo 16, and IRSPGR images with an automated tool (sct_propseg[65,66]) before quality control was performed manually. The cord segmentations were used to rigidly align GRASE echo 1 and IRSPGR with T_2*w cord images. Finally, all images were masked using the higher-resolution T_2*w cord segmentation.

Multivariate template creation was performed by iteratively co-registering the aligned and masked GRASE echo 1, IRSPGR and anatomical images (T_1w for brain, T_2*w for cord) using iterative rigid, affine, and SyN

transformations. Registrations were guided by mutual information (for linear stages) and neighborhood cross-correlation (for SyN) similarity metrics. The T_1w and T_2*w similarity metrics were weighted twice as heavily as those of GRASE and IRSPGR, to account for their better resolution and tissue contrast.

Region of interest definition. A reference anatomical T_1-weighted template was used to generate brain ROIs. This reference template was created in-house using data from 100 healthy volunteers, including those in the current study. After registration between our T_1w template and the reference T_1w template, JHU-ICBM-DTI-81 WM labels and MNI structural regions, optimized for the reference template using the probabilistic joint label fusion framework[67], were transformed to our multivariate template space. Atropos *n*-tissue segmentation was performed on our T_1w template to provide WM and GM segmentations[64].

To generate spinal cord ROIs, registration was performed between our T_2*w spinal cord template and the T_2*-weighted SCT PAM50 template[68], centred at the C2/C3 level of the cord, and refined using a manually defined cord GM segmentation to improve alignment of intra-cord structure. This provided probabilistic cord ROIs, which were thresholded and binarized to only include voxels with probability > 0.5, to reduce partial volume effects.

Multiple sclerosis image analysis. RRMS and PPMS images were processed the same as those of healthy participants, except they were excluded from template creation. Instead, their T_1w and T_2*w images were registered to the T_1w and T_2*w templates, and transformations were concatenated to align their MWF and f_M maps in template space for comparison. Since the goal of the study was not to derive clinical conclusions, images from participants with multiple sclerosis were not segmented into lesion/non-lesion tissue.

Statistical analysis. From the healthy participant MWF maps, aligned in template space, atlases were created by calculating the voxel-wise mean and SD between participants, then cropped to exclude regions not covered by all individual participant MWF and f_M FOV. For the mean MWF and f_M atlases, the mean and SD within each ROI were calculated. Mean MWF and f_M ROI values were compared across all healthy control participants using a paired, two-tailed t test. MWF and f_M Z score maps were calculated by subtracting the mean atlas from the MS participant quantitative map, then dividing by the SD atlas. Z score maps were also masked to exclude highly variable voxels, where the coefficient of variation (calculated voxel-wise as the SD divided by the mean) was over 0.75.

Data availability

Ethics approval did not allow for making individual subjects' imaging data available. However, the anatomical templates, quantitative atlases, and ROIs created and analysed in this study have been made openly available[33] along with example code for the template creation process[69].

Received: 7 September 2020; Accepted: 22 December 2020
Published online: 14 January 2021

References

1. MacKay, A. *et al.* In vivo visualization of myelin water in brain by magnetic resonance. *Magn. Reson. Med.* **31**, 673–677 (1994).
2. Barta, R. *et al.* Modeling T1 and T2 relaxation in bovine white matter. *J. Magn. Reson.* **259**, 56–67 (2015).
3. Bjarnason, T., Vavasour, I., Chia, C. & MacKay, A. Characterization of the NMR behavior of white matter in bovine brain. *Magn. Reson. Med.* **54**, 1072–1081 (2005).
4. Webb, S., Munro, C. A., Midha, R. & Stanisz, G. J. Is multicomponent T2 a good measure of myelin content in peripheral nerve?. *Magn. Reson. Med.* **49**, 638–645 (2003).
5. Laule, C. *et al.* Myelin water imaging in multiple sclerosis: Quantitative correlations with histopathology. *Mult. Scler.* **12**, 747–753. https://doi.org/10.1177/1352458506070928 (2006).
6. Laule, C. *et al.* Myelin water imaging of multiple sclerosis at 7 T: Correlations with histopathology. *Neuroimage* **40**, 1575–1580. https://doi.org/10.1016/j.neuroimage.2007.12.008 (2008).
7. Feinberg, D. A. & Oshio, K. Grase (gradient-echo and spin-echo) MR imaging—A new fast clinical imaging technique. *Radiology* **181**, 597–602 (1991).
8. Prasloski, T. *et al.* Rapid whole cerebrum myelin water imaging using a 3D GRASE sequence. *Neuroimage* **63**, 533–539. https://doi.org/10.1016/j.neuroimage.2012.06.064 (2012).
9. Deoni, S. C., Rutt, B. K., Arun, T., Pierpaoli, C. & Jones, D. K. Gleaning multicomponent T1 and T2 information from steady-state imaging data. *Magn. Reson. Med.* **60**, 1372–1387. https://doi.org/10.1002/mrm.21704 (2008).
10. Miller, K. L., Tijssen, R. H., Stikov, N. & Okell, T. W. Steady-state MRI: Methods for neuroimaging. *Imaging Med.* **3**, 93 (2011).
11. Wiggermann, V. *et al.* Non-negative least squares computation for in vivo myelin mapping using simulated multi-echo spin-echo T2 decay data. *NMR Biomed.* **77**, e4277 (2020).
12. Lankford, C. L. & Does, M. D. On the inherent precision of mcDESPOT. *Magn. Reson. Med.* **69**, 127–136. https://doi.org/10.1002/mrm.24241 (2013).
13. Deoni, S. C. L. & Kolind, S. H. Investigating the stability of mcDESPOT myelin water fraction values derived using a stochastic region contraction approach. *Magn. Reson. Med.* **73**, 161–169 (2014).
14. Bouhrara, M. *et al.* Analysis of mcDESPOT-and CPMG-derived parameter estimates for two-component nonexchanging systems. *Magn. Reson. Med.* **75**, 2406–2420 (2016).
15. West, D. J. *et al.* Inherent and unpredictable bias in multi-component DESPOT myelin water fraction estimation. *Neuroimage* **195**, 78–88 (2019).
16. Poon, C. S. & Henkelman, R. M. Practical T2 quantitation for clinical applications. *J Magn. Reson. Imaging* **2**, 541–553 (1992).
17. Vavasour, I. M., Whittall, K. P., Li, D. K. & MacKay, A. L. Different magnetization transfer effects exhibited by the short and long T(2) components in human brain. *Magn. Reson. Med.* **44**, 860–866 (2000).
18. Does, M. D. & Gore, J. C. Rapid acquisition transverse relaxometric imaging. *J. Magn. Reson.* **147**, 116–120 (2000).
19. Laule, C., Kolind, S. H., Bjarnason, T. A., Li, D. K. & MacKay, A. L. In vivo multiecho T2 relaxation measurements using variable TR to decrease scan time. *Magn. Reson. Imaging* **25**, 834–839. https://doi.org/10.1016/j.mri.2007.02.016 (2007).

20. Deoni, S. C. L. High-resolution T1 mapping of the brain at 3T with driven equilibrium single pulse observation of T1 with high-speed incorporation of RF field inhomogeneities (DESPOT1-HIFI). *J. Magn. Reson. Imaging* **26**, 1106–1111. https://doi.org/10.1002/jmri.21130 (2007).
21. Deoni, S. C. L. Transverse relaxation time (T2) mapping in the brain with off-resonance correction using phase-cycled steady-state free precession imaging. *J. Magn. Reson. Imaging* **30**, 411–417 (2009).
22. Prasloski, T., Madler, B., Xiang, Q. S., MacKay, A. & Jones, C. Applications of stimulated echo correction to multicomponent T2 analysis. *Magn. Reson. Med.* **67**, 1803–1814. https://doi.org/10.1002/mrm.23157 (2012).
23. Deoni, S. C. L., Matthews, L. & Kolind, S. H. One component? Two components? Three? The effect of including a nonexchanging "free" water component in multicomponent driven equilibrium single pulse observation of T1 and T2. *Magn. Reson. Med.* **70**, 147–154 (2012).
24. Zhang, J., Kolind, S. H., Laule, C. & MacKay, A. L. How does magnetization transfer influence mc DESPOT results?. *Magn. Reson. Med.* **74**, 1327–1335 (2015).
25. Zhang, J., Kolind, S. H., Laule, C. & MacKay, A. L. Comparison of myelin water fraction from multiecho T2 decay curve and steady-state methods. *Magn. Reson. Med.* **73**, 223–232 (2015).
26. O'Muircheartaigh, J. *et al.* Quantitative neuroimaging measures of myelin in the healthy brain and in multiple sclerosis. *Hum. Brain Mapp.* **40**, 2104–2116 (2019).
27. Ljungberg, E. *et al.* Rapid myelin water imaging in human cervical spinal cord. *Magn. Reson. Med.* https://doi.org/10.1002/mrm.26551 (2016).
28. Kolind, S. H. & Deoni, S. C. Rapid three-dimensional multicomponent relaxation imaging of the cervical spinal cord. *Magn. Reson. Med.* **65**, 551–556. https://doi.org/10.1002/mrm.22634 (2011).
29. Weber, A. M., Zhang, Y., Kames, C. & Rauscher, A. Myelin water imaging and R2* mapping in neonates: Investigating R2* dependence on myelin and fibre orientation in whole brain white matter. *NMR Biomed.* **33**, e4222 (2020).
30. Deoni, S. C., Dean, D. C. III., O'Muircheartaigh, J., Dirks, H. & Jerskey, B. A. Investigating white matter development in infancy and early childhood using myelin water faction and relaxation time mapping. *Neuroimage* **63**, 1038–1053 (2012).
31. Kolind, S. *et al.* Brain and cord myelin water imaging: A progressive multiple sclerosis biomarker. *Neuroimage Clin.* **9**, 574–580. https://doi.org/10.1016/j.nicl.2015.10.002 (2015).
32. Laule, C. *et al.* Two-year study of cervical cord volume and myelin water in primary progressive multiple sclerosis. *Mult. Scler.* **16**, 670–677. https://doi.org/10.1177/1352458510365586 (2010).
33. Dvorak, A. V. Multivariate MRI templates and myelin imaging atlases for human brain and spinal cord. (2020). https://doi.org/10.5281/zenodo.4157768.
34. Zhang, J., Kolind, S. H., Laule, C. & MacKay, A. L. Comparison of myelin water fraction from multiecho T2 decay curve and steady-state methods. *Magn. Reson. Med.* **73**, 223–232 (2014).
35. Aboitiz, F., Scheibel, A. B., Fisher, R. S. & Zaidel, E. Fiber composition of the human corpus callosum. *Brain Res.* **598**, 143–153 (1992).
36. Bürgel, U., Mecklenburg, I., Blohm, U. & Zilles, K. Histological visualization of long fiber tracts in the white matter of adult human brains. *J. Hirnforsch.* **38**, 397–404 (1997).
37. Bürgel, U. *et al.* White matter fiber tracts of the human brain: Three-dimensional mapping at microscopic resolution, topography and intersubject variability. *NeuroImage* **29**, 1092–1105. https://doi.org/10.1016/j.neuroimage.2005.08.040 (2006).
38. Vavasour, I. M. *et al.* A comparison between magnetization transfer ratios and myelin water percentages in normals and multiple sclerosis patients. *Magn. Reson. Med.* **40**, 763–768 (1998).
39. Smith, M. E. & Sedgewick, L. M. Studies of the mechanism of demyelination regional differences in myelin stability in vitro 1. *J. Neurochem.* **24**, 763–770 (1975).
40. Malik, S. J., Teixeira, R. P. A. & Hajnal, J. V. Extended phase graph formalism for systems with magnetization transfer and exchange. *Magn. Reson. Med.* **80**, 767–779 (2018).
41. Ou, X. & Gochberg, D. F. MT effects and T1 quantification in single-slice spoiled gradient echo imaging. *Magn. Reson. Med.* **59**, 835–845 (2008).
42. Crooijmans, H., Scheffler, K. & Bieri, O. Finite RF pulse correction on DESPOT2. *Magn. Reson. Med.* **65**, 858–862 (2011).
43. Teixeira, A. G. R. P., Malik, S. J. & Hajnal, J. V. Fast quantitative MRI using controlled saturation magnetization transfer. *Magn. Reson. Med.* **81**, 907–920 (2019).
44. Liu, F., Block, W. F., Kijowski, R. & Samsonov, A. Rapid multicomponent relaxometry in steady state with correction of magnetization transfer effects. *Magn. Reson. Med.* **75**, 1423–1433 (2016).
45. Graham, S. J., Stanchev, P. L. & Bronskill, M. J. Criteria for analysis of multicomponent tissue T2 relaxation data. *Magn. Reson. Med.* **35**, 370–378 (1996).
46. Kalantari, S., Komeilizadeh, N., Vavasour, I., Sahebjavaher, R. & MacKay, A. Variation of myelin water fraction as a function of TR. In *Proc. 21st Annual Meeting of ISMRM* (2013).
47. Dula, A. N., Gochberg, D. F., Valentine, H. L., Valentine, W. M. & Does, M. D. Multiexponential T2, magnetization transfer, and quantitative histology in white matter tracts of rat spinal cord. *Magn. Reson. Med.* **63**, 902–909 (2010).
48. Dortch, R. D., Harkins, K. D., Juttukonda, M. R., Gore, J. C. & Does, M. D. Characterizing inter-compartmental water exchange in myelinated tissue using relaxation exchange spectroscopy. *Magn. Reson. Med.* **70**, 1450–1459 (2013).
49. Novikov, D. S., Kiselev, V. G. & Jespersen, S. N. On modeling. *Magn. Reson. Med.* **79**, 3172–3193 (2018).
50. Smith, S. A., Edden, R. A., Farrell, J. A., Barker, P. B. & Van Zijl, P. C. Measurement of T1 and T2 in the cervical spinal cord at 3 tesla. *Magn. Reson. Med.* **60**, 213–219 (2008).
51. Kitzler, H. H. *et al.* Deficient MWF mapping in multiple sclerosis using 3D whole-brain multi-component relaxation MRI. *Neuroimage* **59**, 2670–2677 (2012).
52. Liu, H. *et al.* Myelin water atlas: A template for myelin distribution in the brain. *J. Neuroimaging* **29**, 699 (2018).
53. Dvorak, A. V. *et al.* Rapid myelin water imaging for the assessment of cervical spinal cord myelin damage. *Neuroimage Clin.* **23**, 101896. https://doi.org/10.1016/j.nicl.2019.101896 (2019).
54. Dvorak, A. V. *et al.* Multi-spin echo T2 relaxation imaging with compressed sensing (METRICS) for rapid myelin water imaging. *Magn. Reson. Med.* **84**, 1264 (2020).
55. Thompson, A. J. *et al.* Diagnosis of multiple sclerosis: 2017 revisions of the McDonald criteria. *Lancet Neurol.* **17**, 162–173 (2018).
56. Kurtzke, J. F. Rating neurologic impairment in multiple sclerosis: An expanded disability status scale (EDSS). *Neurology* **33**, 1444–1452 (1983).
57. Pruessmann, K. P., Weiger, M., Scheidegger, M. B. & Boesiger, P. SENSE: Sensitivity encoding for fast MRI. *Magn. Reson. Med.* **42**, 952–962 (1999).
58. Avants, B. B. *et al.* A reproducible evaluation of ANTs similarity metric performance in brain image registration. *Neuroimage* **54**, 2033–2044. https://doi.org/10.1016/j.neuroimage.2010.09.025 (2011).
59. De Leener, B. *et al.* SCT: Spinal cord toolbox, an open-source software for processing spinal cord MRI data. *Neuroimage* **145**, 24–43. https://doi.org/10.1016/j.neuroimage.2016.10.009 (2017).
60. Jenkinson, M., Beckmann, C. F., Behrens, T. E., Woolrich, M. W. & Smith, S. M. Fsl. *Neuroimage* **62**, 782–790 (2012).
61. Tustison, N. J. *et al.* Logical circularity in voxel-based analysis: Normalization strategy may induce statistical bias. *Hum. Brain Mapp.* **35**, 745–759. https://doi.org/10.1002/hbm.22211 (2014).

62. Tustison, N. J. *et al.* N4ITK: Improved N3 bias correction. *IEEE Trans. Med. Imaging* **29**, 1310–1320. https://doi.org/10.1109/Tmi.2010.2046908 (2010).
63. 63Avants, B. B. & Tustison, N. J. *ANTs/ANTsR Brain Templates* (2018).
64. Avants, B. B., Tustison, N. J., Wu, J., Cook, P. A. & Gee, J. C. An open source multivariate framework for n-tissue segmentation with evaluation on public data. *Neuroinformatics* **9**, 381–400. https://doi.org/10.1007/s12021-011-9109-y (2011).
65. De Leener, B., Cohen-Adad, J. & Kadoury, S. Automatic segmentation of the spinal cord and spinal canal coupled with vertebral labeling. *IEEE Trans. Med. Imaging* **34**, 1705–1718 (2015).
66. De Leener, B., Kadoury, S. & Cohen-Adad, J. Robust, accurate and fast automatic segmentation of the spinal cord. *Neuroimage* **98**, 528–536 (2014).
67. Wang, H. & Yushkevich, P. A. Multi-atlas segmentation with joint label fusion and corrective learning-an open source implementation. *Front. Neuroinform.* **7**, 27. https://doi.org/10.3389/fninf.2013.00027 (2013).
68. De Leener, B. *et al.* PAM50: Unbiased multimodal template of the brainstem and spinal cord aligned with the ICBM152 space. *Neuroimage* **165**, 170–179. https://doi.org/10.1016/j.neuroimage.2017.10.041 (2018).
69. Dvorak, A. V. Avdvorak/multivariate-template: version 1.0.0. (2020). https://doi.org/10.5281/zenodo.4157687.

Acknowledgements

We thank the volunteers for their time, and the UBC MRI Research Centre and its MRI technologists for supporting this study, as well as Dr. Sean Deoni and Dr. Douglas Dean for helpful discussion. Adam Dvorak is supported by a Natural Sciences and Engineering Research Council of Canada (NSERC) Alexander Graham Bell Canada Graduate Scholarship. Emil Ljungberg is supported by the Wellcome/EPSRC Centre for Medical Engineering [WT203148/Z/16/Z]. Shannon Kolind is supported by a Michael Smith Foundation for Health Research Scholar award and the Milan and Maureen Ilich Foundation. Additional funding support was provided by NSERC Discovery Grant [F17-05113], a Vancouver Coastal Health Research Institute Innovation and Translational Research Award [F18-00375], and the MS Society of Canada [F16-04023].

Author contributions

A.V.D. was involved in study conception, design, data acquisition, analysis and interpretation, and created the figures, drafted, and substantially revised the work. E.L.J. was involved in study conception, data acquisition, interpretation, and helped draft and substantially revise the work. I.M.V., A.L.M. and S.H.K. contributed to study conception, design, interpretation, and substantial revision. L.E.L. and S.A. contributed to data acquisition and substantial revision. D.K.B.L. and A.T. contributed to study conception and interpretation.

Competing interests

The authors declare no competing interests.

Additional information

Correspondence and requests for materials should be addressed to A.V.D.

Reprints and permissions information is available at www.nature.com/reprints.

Publisher's note Springer Nature remains neutral with regard to jurisdictional claims in published maps and institutional affiliations.